Letter

Stochastic and mixed density functional theory within the projector augmented wave formalism for simulation of warm dense matter

Vidushi Sharma [1,2] Lee A. Collins [1] and Alexander J. White [1,*]

[1]*Theoretical Division, Los Alamos National Laboratory, Los Alamos, New Mexico 87545, USA*
[2]*Center for Nonlinear Studies, Los Alamos National Laboratory, Los Alamos, New Mexico 87545, USA*

Stochastic density functional theory (DFT) and mixed stochastic-deterministic DFT are burgeoning approaches for the calculation of the equation of state and transport properties in materials under extreme conditions. In the intermediate warm dense matter regime, a state between correlated condensed matter and kinetic plasma, electrons can range from being highly localized around nuclei to delocalized over the whole simulation cell. The plane-wave basis pseudopotential approach is thus the typical tool of choice for modeling such systems at the DFT level. Unfortunately, stochastic DFT methods scale as the square of the maximum plane-wave energy in this basis. To reduce the effect of this scaling and improve the overall description of the electrons within the pseudopotential approximation, we present stochastic and mixed DFT approaches developed and implemented within the projector augmented wave formalism. We compare results between the different DFT approaches for both single-point and molecular dynamics trajectories and present calculations of self-diffusion coefficients of solid density carbon from 1 to 50 eV.

The warm dense matter (WDM) regime encompasses a wide variety of extreme environments, providing an excellent testing ground for methods that determine material properties. This includes planetary interiors [1–3], stellar systems such as brown and white dwarfs [4], and the capsule compression stage in inertial confinement fusion (ICF) [5–7]. In ice giant planets, the interiors may support a superionic phase in which hydrogen remains fluid within the lattices of the heavier constituents [8–10], which may help explain the anomalous planetary magnetic fields of Neptune and Uranus. In addition, the difference between an exothermic Neptune and an endothermic Uranus may originate in the nucleation of diamonds from hydrocarbon mixtures [11,12]. Finally, properties such as equations of state and thermal conductivities of various hydrocarbons determine the performance of ICF capsules irradiated by laser pulses [5], and stopping power characterizes the cooling effects of deposition of the capsule material into the hydrogen fuel [13,14]. Activation of the James Webb Space Telescope presages an explosion of discoveries [15] of exoplanets representing a vast range of physical conditions, distributions, and dynamics involving, to list just a few, surface-atmosphere couplings [16], interfaces between solid and liquid components of interiors [17], and formation pathways [18]. The breakthrough fusion milestone [19] at the National Ignition Facility emphasizes the role played in modeling by ever-improved basic physical attributes. Recent developments signal a pressing need for more accurate microscopic properties over a broad range of WDM conditions.

Many methods exist to determine the basic structure and dynamics of WDM; the most accurate arise from first-principles techniques such as density functional theory (DFT) [20–22] and path integral Monte Carlo [23,24], which supply a consistent set of basic material properties such as equations of state, opacities, mass transport, and electrical and thermal conduction. Recently, DFT simulations have provided training information to determine model potentials from machine learning techniques [10,11,25,26]. Kohn-Sham (KS) DFT combined with the plane-wave pseudopotential (PWPP) method is the theory of choice for studying the electronic structure of numerous materials, ranging from solid-state condensed matter to hot dense plasmas. The success of DFT stems from the balance between computational complexity and useful accuracy, achieved by replacing the quantum-mechanical wave function by a much simpler quantity: The KS density matrix, typically constructed from the KS Hamiltonian eigenstates.

Cubic scaling of the computational complexity of KS-DFT with respect to both system size and temperature is a major limitation [27]. For WDM systems, orbital-free DFT has been a particularly useful alternative, but it is based on an approximate treatment of the electron noninteracting kinetic energy [28–30]. Linear scaling methods, such as stochastic DFT (SDFT) [31], provide a full KS accuracy alternative for large or hot systems [32]. Mixed stochastic-deterministic DFT (MDFT) shows great promise for providing full KS-DFT accuracy for calculations at any temperature [33]. However, when combined with the PWPP method, SDFT, and by extension MDFT, has a quadratic dependence of the computational cost on the maximum plane-wave energy E_{cut}, i.e., on the grid resolution, compared to standard deterministic DFT's linear dependence. Moreover, it has been formulated only in combination with norm-conserving pseudopotentials, which either show low accuracy or require higher E_{cut}. High

*alwhite@lanl.gov

accuracy and low E_{cut} can be achieved using soft pseudopotentials, first developed by Vanderbilt [34], leading to a nonorthogonal basis. However, the orbitals from either the norm-conserving or "ultrasoft" pseudopotentials are not the true KS orbitals. This is critical for calculation of optical transitions, particularly involving core electrons, e.g., x-ray absorption near-edge structure spectra [35,36].

The projector augmented wave (PAW) approach, introduced by Blöchl [37] and reformulated by Kresse and Joubert [38], generalizes the soft pseudopotentials to an "all-electron" formalism. The PAW method provides a realistic description of core electrons, provides access to the full KS orbitals, has a long and continued history of development, and yields accuracy comparable to more expensive all-electron methods [39]. Moreover, it allows for very low E_{cut}, suitable for SDFT or MDFT. In this Letter, we develop MDFT, and SDFT by limitation, within the PAW formalism and present isochoric calculations and analysis for carbon spanning the WDM regime, 1 to 50 eV. Recently, White and Collins [33] proposed the MDFT method that generalizes stochastic and deterministic KS-DFT approaches and improves the computational complexity over a wide range of temperatures. It is based on partitioning the full eigenspectrum of $\widehat{H}_{\text{DFT}}$ into low-energy and high-energy segments such that the maximally occupied low-energy eigenstates $|\psi\rangle$ are explicitly resolved while the higher-energy states are spanned by random stochastic vectors $|\chi\rangle$ (see Refs. [31,32,40–42]). We thus form complementary stochastic vectors (CSVs):

$$|\chi'_a\rangle = \left(\widehat{I} - \sum_{b\in N_\psi} |\psi_b\rangle\langle\psi_b|\right)|\chi_a\rangle, \tag{1}$$

where $|\psi_b\rangle$ is an eigenvector of $\widehat{H}_{\text{DFT}}$ with eigenenergy ε_b. We define "occupied" CSVs, $X' = f^{\frac{1}{2}}(\widehat{H}_{\text{DFT}})\chi'$, to obtain the mixed density matrix as

$$\widehat{\rho} = \sum_{a\in N_\chi} |X'_a\rangle\langle X'_a| + \sum_{b\in N_\psi} |\psi_b\rangle f(\varepsilon_b)\langle\psi_b|, \tag{2}$$

where f is the Fermi-Dirac operator. KS-DFT and SDFT are, respectively, limits of MDFT where N_χ or N_ψ is zero. All observables can be expressed as traces over appropriate operators with this density matrix; see [33] for a detailed description.

Figure 1 shows the density of states (DOS) and occupied DOS for a disordered carbon system, obtained with KS-DFT ($N_\psi = 1024$), SDFT ($N_\chi = 256$), and MDFT ($N_\psi/N_\chi = 128/16$). The low-energy deterministic component of MDFT is shown in pink, and there is overall good agreement across the three methods. The overlap of the components is due to the finite width of Gaussian functions used to define the continuous DOS.

The PAW formalism is based on a linear transformation matrix $\widehat{\tau}$ connecting the smooth transformed density matrix $\widetilde{\rho}$ to an all-electron density matrix $\widehat{\rho}$,

$$\widehat{\rho} = \widehat{\tau}\,\widetilde{\rho}\,\widehat{\tau}^\dagger, \tag{3}$$

$$\widehat{\tau} = \widehat{I} + \sum_i (|\phi_i\rangle - |\widetilde{\phi}_i\rangle)\langle p_i|, \tag{4}$$
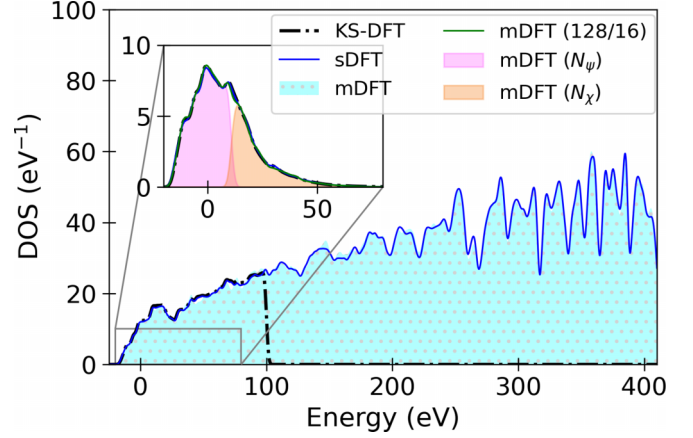

FIG. 1. Disordered 64-carbon system at $(\rho, T) = (3.52 \text{ g/cm}^3, 10 \text{ eV})$: Density of states (DOS) and occupied DOS (inset) obtained with the KS-DFT ($N_\psi = 1024$), SDFT ($N_\chi = 256$), and MDFT ($N_\psi = 128$, $N_\chi = 16$) methods. The chemical potential of the system is $\mu = 7.92$ eV. The pink (left) and orange (right) shaded regions indicate the splitting of deterministic and stochastic subspaces in MDFT.

with $\langle p_i|\widetilde{\phi}_j\rangle = \delta_{ij}$. Here, $|\phi_i\rangle$ is an all-electron partial wave, and $|\widetilde{\phi}_i\rangle$ is a pseudo partial wave dual to the projector $|p_i\rangle$. This transformation is exact for a complete set of partial waves and projectors [37,38]. These functions are limited to localized "augmentation spheres" around each atom. Observables are preserved by defining pseudized operators $\widetilde{O}$ as

$$E[\widehat{O}] = \text{Tr}[\widehat{\rho}\,\widehat{O}] = \text{Tr}[\widetilde{\rho}\,\widetilde{O}], \quad \widetilde{O} = \widehat{\tau}^\dagger\widehat{O}\widehat{\tau}. \tag{5}$$

The transformed identity operator gives an S-orthogonality condition for the transformed wave functions:

$$\widehat{S} = \widehat{\tau}^\dagger\widehat{\tau} = \widehat{I} + \sum_{i,j} |p_i\rangle(\langle\phi_i|\phi_j\rangle - \langle\widetilde{\phi}_i|\widetilde{\phi}_j\rangle)\langle p_j|, \tag{6}$$

$$\langle\psi_a|\psi_b\rangle = \langle\widetilde{\psi}_a|\widehat{S}|\widetilde{\psi}_b\rangle = \delta_{ab}. \tag{7}$$

Therefore, $\widetilde{\psi}_b$ is a solution to the generalized eigenvalue problem, $\widetilde{H}_{\text{KS}}\widetilde{\psi} = \varepsilon\widehat{S}\widetilde{\psi}$. This S-orthogonality condition complicates the generation of transformed stochastic vectors.

Our approximate projections via all-electron or norm-conserving and transformed vectors is given by

$$\widehat{I} \approx \sum_{a\in N_\chi} |\chi'_a\rangle\langle\chi'_a| + \sum_{b\in N_\psi} |\psi_b\rangle\langle\psi_b|$$
$$= \sum_{a\in N_\chi} \widehat{\tau}|\widetilde{\chi}'_a\rangle\langle\widetilde{\chi}'_a|\widehat{\tau}^\dagger + \sum_{b\in N_\psi} \widehat{\tau}|\widetilde{\psi}_b\rangle\langle\widetilde{\psi}_b|\widehat{\tau}^\dagger. \tag{8}$$

From the vector transformations, the identity operator [Eq. (8)], and the $\widehat{S}$ operator [Eq. (6)], we find that

$$\widehat{S} = \widehat{\tau}^\dagger\widehat{I}\widehat{\tau} \approx \widehat{S}\left(\sum_{a\in N_\chi} |\widetilde{\chi}'_a\rangle\langle\widetilde{\chi}'_a| + \sum_{b\in N_\psi} |\widetilde{\psi}_b\rangle\langle\widetilde{\psi}_b|\right)\widehat{S},$$

$$\widehat{S}^{-1} \approx \sum_{a\in N_\chi} |\widetilde{\chi}'_a\rangle\langle\widetilde{\chi}'_a| + \sum_{b\in N_\psi} |\widetilde{\psi}_b\rangle\langle\widetilde{\psi}_b|. \tag{9}$$

For the moment we assume $N_\psi = 0$ and determine the form of $|\widetilde{\chi}_a\rangle$. We define a set of stochastic vectors $|\bar{\chi}_a\rangle$ such

that $\langle \vec{r} | \widehat{I} | \vec{r}' \rangle = \delta(\vec{r}, \vec{r}') \approx \sum_a \langle \vec{r} | \bar{\chi}_a \rangle \langle \bar{\chi}_a | \vec{r}' \rangle$, which has the same form as the all-electron stochastic vectors [33], but with $\vec{r}$ and $\vec{r}'$ from the coarser grid of the transformed functions [32]. Using the identity $\widehat{I} = \widehat{\tau}\widehat{S}^{-1}\widehat{\tau}^{\dagger}$ (see the Supplemental Material [43], Eq. (S8)) and Eq. (8), we obtain

$$\widehat{I} \approx \sum_a \widehat{\tau}\widehat{S}^{-\frac{1}{2}}|\bar{\chi}_a\rangle\langle\bar{\chi}_a|\widehat{S}^{-\frac{1}{2}}\widehat{\tau}^{\dagger} = \sum_a \widehat{\tau}|\tilde{\chi}_a\rangle\langle\tilde{\chi}_a|\widehat{\tau}^{\dagger},$$

$$|\tilde{\chi}_a\rangle = \widehat{S}^{-\frac{1}{2}}|\bar{\chi}_a\rangle. \quad (10)$$

A computationally efficient and sufficiently accurate $\widehat{S}^{-\frac{1}{2}}$ was formulated recently by Li and Neuhauser [44]. Using the same identity, the pseudized density matrix can be written as (see the Supplemental Material [43])

$$\widetilde{\rho} = f(\widehat{S}^{-1}\widetilde{H}_{\mathrm{KS}})\widehat{S}^{-1},$$

$$= f^{\frac{1}{2}}(\widehat{S}^{-1}\widetilde{H}_{\mathrm{KS}})\widehat{S}^{-1}f^{\frac{1}{2}}(\widetilde{H}_{\mathrm{KS}}\widehat{S}^{-1}). \quad (11)$$

The procedure for PAW MDFT is similar to the all-electron or norm-conserving case [33] with three modifications: (i) the orthogonal stochastic vectors $\bar{\chi}$ are generated and rotated to the standard PAW frame $\tilde{\chi}$, (ii) the generalized eigenvalue problem is iteratively solved to obtain $\tilde{\psi}$, and (iii) the CSVs are formed via

$$|\tilde{\chi}_a'\rangle = \left(\widehat{S}^{-1} - \sum_{b \in N_\psi} |\tilde{\psi}_b\rangle\langle\tilde{\psi}_b|\right)\widehat{S}|\tilde{\chi}_a\rangle, \quad (12)$$

giving

$$\widetilde{\rho} = \sum_{a \in N_\chi} |\tilde{X}_a'\rangle\langle\tilde{X}_a'| + \sum_{b \in N_\psi} |\tilde{\psi}_b\rangle f(\varepsilon_b)\langle\tilde{\psi}_b|, \quad (13)$$

with

$$|\tilde{X}_a'\rangle = f^{\frac{1}{2}}(\widehat{S}^{-1}\widetilde{H}_{\mathrm{KS}})|\tilde{\chi}_a'\rangle. \quad (14)$$

In Eq. (14), S^{-1} can be applied via the Woodbury formula [45]. The observables necessary to complete the PAW formalism, e.g., the on-site density matrix and compensation charge density, can be calculated from Eq. (13). The generalization of PAW forces and stress tensor for MDFT and SDFT is presented in Sec. S2 in the Supplemental Material [43].

Using our open-source [46] PWPP DFT code SHRED (Stochastic and Hybrid Representation Electronic Structure by Density Functional Theory) [47], we perform single-point ground-state energy calculations on 64-atom disordered carbon at a solid-state density of 3.52 g/cm³ with the $4e^-$ PAW potential. Figure 2 shows a comparison of the three DFT algorithms in terms of computational time per self-consistent field (SCF) cycle on 128 CPUs and the accuracy and precision of pressure referenced to the SESAME 7833 value [48]. The free energy, pressure, and chemical potential for each temperature, along with the combination of orbitals N_ψ/N_χ, are listed in Table S1 in the Supplemental Material [43]. The combinations range from 136/4 at $k_BT = 1$ eV to 64/40 at $k_BT = 50$ eV, whereas SDFT times are computed with $N_\chi = 128$ for all temperatures. The pressures in SDFT and MDFT are computed as averages over 10 independent SCF runs using a different set of N_χ stochastic orbitals, with the statistical error (the error bars) expressed as the standard deviation of the sample. The nonlinear nature of the SCF cycle leads to a potential
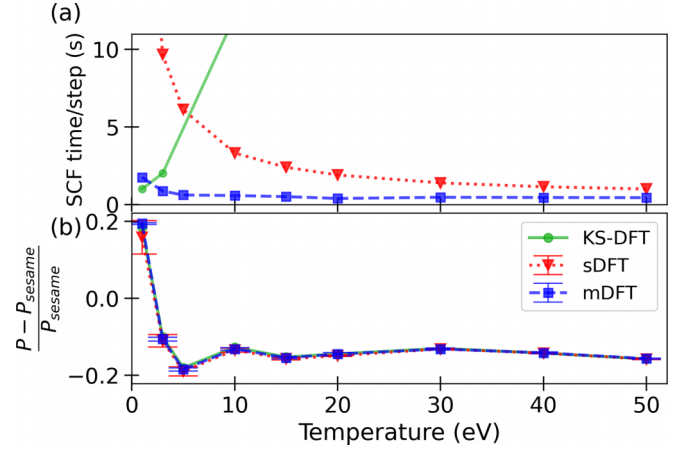

FIG. 2. Disordered 64-carbon snapshot at $\rho = 3.52$ g/cm³. Comparison of (a) SCF times per cycle and (b) relative pressure with reference to SESAME 7833 P_{sesame} [48] obtained for Kohn-Sham, stochastic, and mixed DFT calculations.

bias in SDFT and MDFT given by the difference between the expected value and the KS-DFT result. Mixed DFT yields energies within 0.2% (standard deviation of 0.3%) of the reference KS-DFT values with a 42-fold speedup compared to KS-DFT at $T = 20$ eV. Additionally, the chemical potential and pressure are converged to 0.13 eV (standard deviation of 0.18 eV) and 7.27 GPa (standard deviation of 8.29 GPa) relative to their respective KS-DFT results. Electronic nuclear forces depend on the local electronic density and hence do not benefit from the self-averaging effect of SDFT [40]. A comparison of stochastic and mixed DFT forces for several N_ψ/N_χ is presented in Fig. 3, where $F_{\alpha,n}^{i,\psi\chi}$ ($F_\alpha^{i,\psi}$) indicates mixed or stochastic (deterministic KS) forces, such that $i = \{x, y, z\}, \alpha = 1, \ldots, N_{at}$ indexes the atoms, and $n = 1, \ldots, 10$ indexes the stochastic or mixed run. The absence of an i, n,
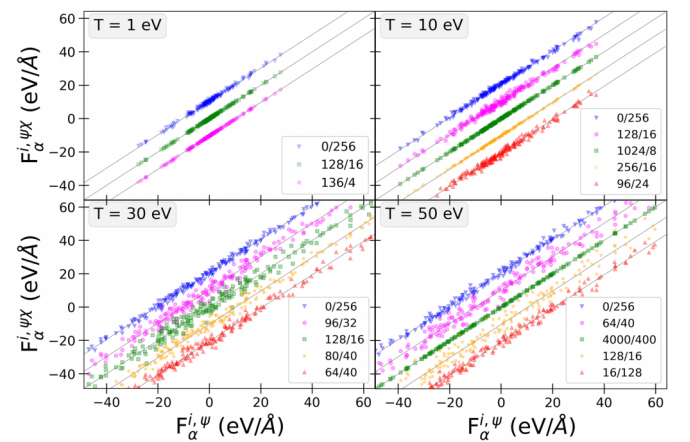

FIG. 3. Comparison of mixed ($F_\alpha^{i,\psi\chi}$) vs Kohn-Sham ($F_\alpha^{i,\psi}$) DFT components of forces on all atoms obtained for various N_ψ/N_χ. The agreement between stochastic (0/256, blue triangles) and deterministic forces improves at higher temperatures. The data points shown by magenta circles represent the chosen N_ψ/N_χ for mixed DFT calculations at a given temperature. At higher temperatures, the area of the force plots is zoomed in to keep a constant scale. The order of lines at each T matches the key.

or α index indicates the magnitude of force, averaged value over 10 independent stochastic or mixed runs, or averaged value over atoms, respectively. The standard deviation over n independent runs averaged over the atoms is given by

$$\sigma^{\psi\chi} = \sum_{\alpha=1}^{N_{at}} N_{at}^{-1} \sqrt{\sum_{n=1}^{10} \frac{\left(F_{\alpha,n}^{\psi\chi} - F_{\alpha}^{\psi}\right)^2}{10}}; \qquad (15)$$

also see Table S2 in the Supplemental Material [43]. Upon comparing the bias in mixed forces ($|F^{\psi\chi} - F^{\psi}|$) with the statistical error $\sigma^{\psi\chi}$, one finds that the largest magnitude of the force bias across temperatures is 1.280 eV/Å, which is smaller than the largest magnitude of the statistical error, 10.471 eV/Å, as expected [49].

Figure 3 shows a comparison of the components of MDFT and SDFT forces $F_{\alpha}^{i,\psi\chi}$ obtained for several N_{ψ}/N_{χ} with the Kohn-Sham forces $F_{\alpha}^{i,\psi}$. The displacement in the mixed forces about the linear curve indicates a statistical error that diminishes with an increasing N_{χ} at higher temperatures. At a given temperature, the data points shown in magenta (circles) indicate the mixed forces for N_{ψ}/N_{χ} employed elsewhere in this work. The forces at $T = (30, 50)$ eV are in good agreement between MDFT and KS-DFT with standard deviations of 8.647 and 10.364 eV/Å, respectively. These can be viewed in conjunction with the purely stochastic forces shown in blue. At lower temperatures, increasing the number of deterministic KS orbitals reduces the fluctuations in forces; for example, at $T = 10$ eV, increasing N_{ψ} from 128/16 (magenta circles) to 256/16 (yellow stars) improves the distribution of forces significantly. However, at moderate to high temperatures one would require a drastically large N_{ψ} to obtain accurate forces (see $T = 50$ eV in Fig. 3). Hence, it is advantageous to increase N_{χ} and decrease N_{ψ} as the temperature increases [33], as evidenced by the forces obtained with $N_{\psi}/N_{\chi} = 128/16$ vs 16/128 at $T = 50$ eV.

The magnitude of force averaged over all atoms $\langle F_{\alpha} \rangle$ is computed with mixed and KS-DFT methods, as shown in Fig. 4(a). The error bars denote the standard deviation in the MDFT forces $\sigma^{\psi\chi}$, and the blue shaded band indicates a thermal fluctuation region described by a Langevin-type fluctuation ς such that

$$m_{\alpha} \ddot{q}_{\alpha} = f_{\alpha} - \gamma_{\alpha} p_{\alpha} + \varsigma \eta_{\alpha}(t), \qquad (16)$$

where $\varsigma \equiv \sqrt{2 m_{\alpha} \gamma_{\alpha} k_B T}$, q_{α} and p_{α} are the coordinates and momenta of the atoms, f_{α} is the force on the atom, γ_{α} is the damping constant, and $\eta_{\alpha}(t)$ is a Gaussian process such that $\langle \eta_{\alpha}(t) \rangle = 0$ and $\langle \eta_{\alpha}(t) \eta_{\alpha'}(t') \rangle = \delta_{\alpha\alpha'} \delta(t - t')$. Langevin molecular dynamics was successfully used to investigate forces from SDFT-based simulations [49,50]. At a given temperature, $\langle F_{\alpha} \rangle \pm 2\varsigma$ is explicitly computed and interpolated to yield the thermal-fluctuation band in Fig. 4(a). The averaged MDFT forces along with the error bars are contained within the thermal band. This shows that the statistical error as captured quantitatively by $\sigma^{\psi\chi}$ and qualitatively in Fig. 3 can be absorbed by the thermal fluctuations in dynamical simulations. While the statistical fluctuations are contained within 2ς, the bias in the forces lies within 1ς, indicating that accuracy converges faster than precision [32].

In order to investigate the effect of these relatively small biases on observables, we apply MDFT to compute transport
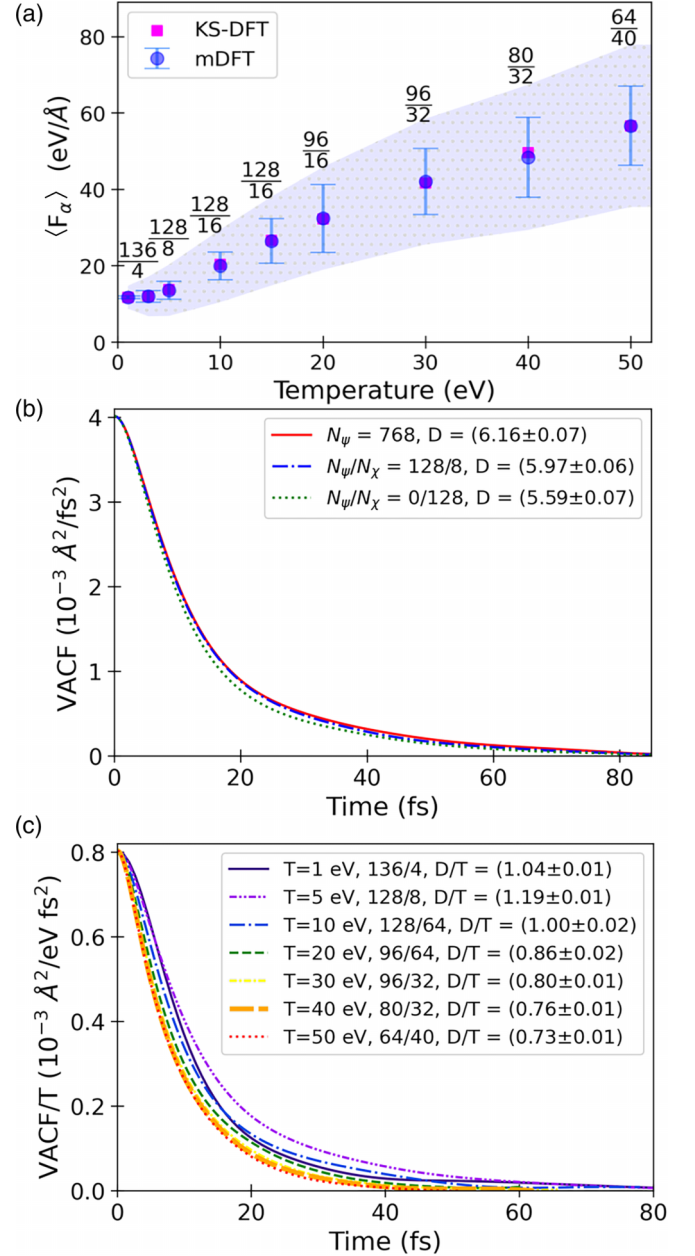

FIG. 4. Disordered 64-carbon system at $\rho = 3.52$ g/cm^3: Average magnitude of force on atoms $\langle F_{\alpha} \rangle$ obtained with KS- and mixed DFT for a single snapshot. For KS-DFT, N_{ψ} ranges from 256 at $T = 1$ eV to 6400 at $T = 50$ eV. The error bars indicate the statistical error over mixed DFT runs, and the shaded region represents a Langevin-type friction term at the respective temperature, $\langle F_{\alpha} \rangle \pm 2\varsigma$, with $\gamma_{\alpha} = 0.04$ fs^{-1} [50]. A comparison of (b) the velocity autocorrelation function (VACF) for KS- (solid line), mixed (dash-dotted line), and stochastic (dotted line) DFT methods at $T = 5$ eV and (c) VACF/T at different temperatures T. The self-diffusion coefficients D (integral of VACF) are given in the key in units of 10^{-3} cm^2/s.

properties via molecular dynamics (MD) simulations. We employ an isokinetic [51] ensemble that is typically used for WDM transport calculations [29,30]. The time-averaged free energy and total pressure along with their standard deviations are given in Table S3 in the Supplemental Material [43]. We

compute the velocity autocorrelation function (VACF) and self-diffusion coefficient D [29,30,52] of carbon with KS-, mixed, and stochastic DFT [see Fig. 4(b)]. The finite simulation time in MD results in a statistical error, in addition to that due to the stochasticity in SDFT and MDFT. We see the average MDFT diffusion coefficients fall between 1 and 2 times the statistical error estimate, which is within the range of reasonable estimates (see the Supplemental Material [43]). The pure SDFT diffusion coefficient falls slightly outside this range but is still within 10% of the deterministic case.

Figure 4(c) shows a comparison of temperature-scaled VACF and D for several T, with N_ψ/N_χ specified in the key. The relationship between D and T over a temperature range at any given density was previously investigated for high-Z materials that exhibit multiple ionization states [53]. It was argued that, over a large temperature and density range, the mutually compensating effects of increased ionization and thermal energy result in a constant coupling parameter Γ, giving rise to a so-called Γ plateau which, in turn, affects quantities such as self-diffusion and viscosity. We see that for 1 to 5 eV the change in temperature dominates correlation, leading to an increase in D/T, while for greater than 5 eV the ionization effects become significant, leading to a decrease in D/T.

We have developed and implemented the MDFT and SDFT methods within the plane-wave PAW formalism for DFT. The PAW formalism provides a significant acceleration of stochastic DFT methods due to both smaller grids and a decreased eigenspectrum range. Additionally, it opens the door to efficient, all-electron accuracy, calculations of matter in extreme conditions like those possible in ambient conditions [39]. We have demonstrated the efficacy of this approach in the simulation of transport properties in isochorically heated warm dense carbon up to 50 eV, observing the crossover from kinetically to Coulomb-dominated correlation effects. Future work will include additional transport studies and application of the PAW method to time-dependent MDFT and optical response via the Kubo-Greenwood approach.

[1] National Academies of Sciences, Engineering, and Medicine, *Exoplanet Science Strategy* (National Academies Press, Washington, DC, 2018).

[2] M. Bethkenhagen, E. R. Meyer, S. Hamel, N. Nettelmann, M. French, L. Scheibe, C. Ticknor, L. A. Collins, J. D. Kress, J. J. Fortney, and R. Redmer, Planetary ices and the linear mixing approximation, Astrophys. J. **848**, 67 (2017).

[3] N. A. Teanby, P. G. J. Irwin, J. I. Moses, and R. Helled, Neptune and Uranus: Ice or rock giants? Philos. Trans. R. Soc. A **378**, 20190489 (2020).

[4] A. Becker, M. Bethkenhagen, C. Kellermann, J. Wicht, and R. Redmer, Material properties for the interiors of massive giant planets and brown dwarfs, Astronom. J. **156**, 149 (2018).

[5] S. X. Hu, L. A. Collins, T. R. Boehly, Y. H. Ding, P. B. Radha, V. N. Goncharov, V. V. Karasiev, G. W. Collins, S. P. Regan, and E. M. Campbell, A review on *ab initio* studies of static, transport, and optical properties of polystyrene under extreme conditions for inertial confinement fusion applications, Phys. Plasmas **25**, 056306 (2018).

[6] A. Fernandez-Pañella, M. Millot, D. E. Fratanduono, M. P. Desjarlais, S. Hamel, M. C. Marshall, D. J. Erskine, P. A. Sterne, S. Haan, T. R. Boehly, G. W. Collins, J. H. Eggert, and P. M. Celliers, Shock Compression of Liquid Deuterium up to 1 TPa, Phys. Rev. Lett. **122**, 255702 (2019).

[7] B. Bachmann *et al.*, Measurement of Dark Ice-Ablator Mix in Inertial Confinement Fusion, Phys. Rev. Lett. **129**, 275001 (2022).

[8] M. Millot, S. Hamel, J. R. Rygg, P. M. Celliers, G. W. Collins, F. Coppari, D. E. Fratanduono, R. Jeanloz, D. C. Swift, and J. H. Eggert, Experimental evidence for superionic water ice using shock compression, Nat. Phys. **14**, 297 (2018).

[9] B. Cheng, M. Bethkenhagen, C. J. Pickard, and S. Hamel, Phase behaviours of superionic water at planetary conditions, Nat. Phys. **17**, 1228 (2021).

[10] H. Gao, C. Liu, J. Shi, S. Pan, T. Huang, X. Lu, H.-T. Wang, D. Xing, and J. Sun, Superionic Silica-Water and Silica-Hydrogen Compounds in the Deep Interiors of Uranus and Neptune, Phys. Rev. Lett. **128**, 035702 (2022).

[11] B. Cheng, S. Hamel, and M. Bethkenhagen, Thermodynamics of diamond formation from hydrocarbon mixtures in planets, Nat. Commun. **14**, 1104 (2023).

[12] M. Ross, The ice layer in Uranus and Neptune–Diamonds in the sky? Nature (London) **292**, 435 (1981).

[13] A. J. White, O. Certik, Y. H. Ding, S. X. Hu, and L. A. Collins, Time-dependent orbital-free density functional theory for electronic stopping power: Comparison to the Mermin-Kohn-Sham theory at high temperatures, Phys. Rev. B **98**, 144302 (2018).

[14] Y. H. Ding, A. J. White, S. X. Hu, O. Certik, and L. A. Collins, *Ab initio* Studies on the Stopping Power of Warm Dense Matter with Time-Dependent Orbital-Free Density Functional Theory, Phys. Rev. Lett. **121**, 145001 (2018).

[15] E.-M. Ahrer, L. Alderson, N. M. Batalha, N. E. Batalha, J. L. Bean, T. G. Beatty, T. J. Bell, B. Benneke, Z. K. Berta-Thompson, A. L. Carter, I. J. M. Crossfield *et al.*, Identification of carbon dioxide in an exoplanet atmosphere, Nature (London) **614**, 649 (2023).

[16] W. Dietrich, S. Kumar, A. J. Poser, M. French, N. Nettelmann, R. Redmer, and J. Wicht, Magnetic induction processes in hot Jupiters, application to KELT-9b, Mon. Not. R. Astron. Soc. **517**, 3113 (2022).

[17] Y. Miyazaki and D. J. Stevenson, A subsurface magma ocean on Io: Exploring the steady state of partially molten planetary bodies, Planet. Sci. J. **3**, 256 (2022).

[18] S.-F. Liu, Y. Hori, S. Müller, X. Zheng, R. Helled, D. Lin, and A. Isella, The formation of Jupiter's diluted core by a giant impact, Nature (London) **572**, 355 (2019).

[19] A. B. Zylstra, O. A. Hurricane, D. A. Callahan, A. L. Kritcher, J. E. Ralph, H. F. Robey, J. S. Ross, C. V. Young, K. L. Baker, D. T. Casey, T. Döppner *et al.*, Burning plasma achieved in inertial fusion, Nature (London) **601**, 542 (2022).

[20] W. Kohn and L. J. Sham, Self-Consistent Equations Including Exchange and Correlation Effects, Phys. Rev. **140**, A1133 (1965).

[21] A. Pribram-Jones, S. Pittalis, E. K. U. Gross, and K. Burke, Thermal density functional theory in context, in *Frontiers and Challenges in Warm Dense Matter*, edited by F. Graziani, M. P. Desjarlais, R. Redmer, and S. B. Trickey (Springer, Cham, 2014), pp. 25–60.

[22] M. Bonitz, T. Dornheim, Z. A. Moldabekov, S. Zhang, P. Hamann, H. Kählert, A. Filinov, K. Ramakrishna, and J. Vorberger, *Ab initio* simulation of warm dense matter, Phys. Plasmas **27**, 042710 (2020).

[23] D. M. Ceperley, Path integrals in the theory of condensed helium, Rev. Mod. Phys. **67**, 279 (1995).

[24] K. P. Driver and B. Militzer, All-Electron Path Integral Monte Carlo Simulations of Warm Dense Matter: Application to Water and Carbon Plasmas, Phys. Rev. Lett. **108**, 115502 (2012).

[25] V. L. Deringer, M. A. Caro, and G. Csányi, Machine learning interatomic potentials as emerging tools for materials science, Adv. Mater. **31**, 1902765 (2019).

[26] H.-F. Li, A. R. Oganov, H. Cui, X.-F. Zhou, X. Dong, and H.-T. Wang, Ultrahigh-Pressure Magnesium Hydrosilicates as Reservoirs of Water in Early Earth, Phys. Rev. Lett. **128**, 035703 (2022).

[27] A. Blanchet, M. Torrent, and J. Clérouin, Requirements for very high temperature Kohn–Sham DFT simulations and how to bypass them, Phys. Plasmas **27**, 122706 (2020).

[28] F. Lambert, J. Clérouin, and S. Mazevet, Structural and dynamical properties of hot dense matter by a Thomas-Fermi-Dirac molecular dynamics, Europhys. Lett. **75**, 681 (2006).

[29] C. Ticknor, J. D. Kress, L. A. Collins, J. Clérouin, P. Arnault, and A. Decoster, Transport properties of an asymmetric mixture in the dense plasma regime, Phys. Rev. E **93**, 063208 (2016).

[30] A. J. White, L. A. Collins, J. D. Kress, C. Ticknor, J. Clérouin, P. Arnault, and N. Desbiens, Correlation and transport properties for mixtures at constant pressure and temperature, Phys. Rev. E **95**, 063202 (2017).

[31] M. D. Fabian, B. Shpiro, E. Rabani, D. Neuhauser, and R. Baer, Stochastic density functional theory, Wiley Interdiscip. Rev.: Computat. Molecular Sci. **9**, e1412 (2019).

[32] Y. Cytter, E. Rabani, D. Neuhauser, and R. Baer, Stochastic density functional theory at finite temperatures, Phys. Rev. B **97**, 115207 (2018).

[33] A. J. White and L. A. Collins, Fast and Universal Kohn-Sham Density Functional Theory Algorithm for Warm Dense Matter to Hot Dense Plasma, Phys. Rev. Lett. **125**, 055002 (2020).

[34] K. Laasonen, A. Pasquarello, R. Car, C. Lee, and D. Vanderbilt, Car-Parrinello molecular dynamics with Vanderbilt ultrasoft pseudopotentials, Phys. Rev. B **47**, 10142 (1993).

[35] M. Taillefumier, D. Cabaret, A.-M. Flank, and F. Mauri, X-ray absorption near-edge structure calculations with the pseudopotentials: Application to the K edge in diamond and α-quartz, Phys. Rev. B **66**, 195107 (2002).

[36] N. Brouwer, V. Recoules, N. Holzwarth, and M. Torrent, Calculation of optical properties with spin-orbit coupling for warm dense matter, Comput. Phys. Commun. **266**, 108029 (2021).

[37] P. E. Blöchl, Projector augmented-wave method, Phys. Rev. B **50**, 17953 (1994).

[38] G. Kresse and D. Joubert, From ultrasoft pseudopotentials to the projector augmented-wave method, Phys. Rev. B **59**, 1758 (1999).

[39] K. Lejaeghere, G. Bihlmayer, T. Björkman, P. Blaha, S. Blügel, V. Blum, D. Caliste, I. E. Castelli, S. J. Clark, A. D. Corso, S. de Gironcoli *et al.*, Reproducibility in density functional theory calculations of solids, Science **351**, aad3000 (2016).

[40] R. Baer, D. Neuhauser, and E. Rabani, Self-Averaging Stochastic Kohn-Sham Density-Functional Theory, Phys. Rev. Lett. **111**, 106402 (2013).

[41] D. Neuhauser, R. Baer, and E. Rabani, Communication: Embedded fragment stochastic density functional theory, J. Chem. Phys. **141**, 041102 (2014).

[42] R. Baer, D. Neuhauser, and E. Rabani, Stochastic Vector Techniques in Ground-State Electronic Structure, Annu. Rev. Phys. Chem. **73**, 255 (2022).

[43] See Supplemental Material at http://link.aps.org/supplemental/10.1103/PhysRevE.108.L023201 for the derivation of the identity operator, density matrix, stress tensor, and forces in PAW formalism; the combination of mixed deterministic-stochastic orbitals; magnitude of forces and stochastic errors; energies and pressures in molecular dynamics along with their standard deviations; and the error estimation procedure for the velocity autocorrelation function. It also includes Refs. [54–57].

[44] W. Li and D. Neuhauser, Real-space orthogonal projector-augmented-wave method, Phys. Rev. B **102**, 195118 (2020).

[45] A. Levitt and M. Torrent, Parallel eigensolvers in plane-wave density functional theory, Comput. Phys. Commun. **187**, 98 (2015).

[46] A. White, SHRED, https://github.com/lanl/shred.

[47] SHRED (Stochastic and Hybrid Representation Electronic structure by Density Functional Theory) is a plane-wave DFT code employing Kohn-Sham, orbital-free, stochastic, and mixed stochastic-deterministic DFT methods.

[48] B. Bennett, J. Johnson, G. Kerley, and G. Rood, Recent developments in the Sesame equation-of-state library, Los Alamos National Laboratory, Report No. LA-7130, 1978, doi:https://doi.org/10.2172/5150206.

[49] B. Shpiro, M. D. Fabian, E. Rabani, and R. Baer, Forces from stochastic density functional theory under nonorthogonal atom-centered basis sets, J. Chem. Theory Comput. **18**, 1458 (2022).

[50] E. Arnon, E. Rabani, D. Neuhauser, and R. Baer, Efficient Langevin dynamics for "noisy" forces, J. Chem. Phys. **152**, 161103 (2020).

[51] P. Minary, G. J. Martyna, and M. E. Tuckerman, Algorithms and novel applications based on the isokinetic ensemble. II. *Ab initio* molecular dynamics, J. Chem. Phys. **118**, 2527 (2003).

[52] E. R. Meyer, J. D. Kress, L. A. Collins, and C. Ticknor, Effect of correlation on viscosity and diffusion in molecular-dynamics simulations, Phys. Rev. E **90**, 043101 (2014).

[53] J. Clérouin, G. Robert, P. Arnault, J. D. Kress, and L. A. Collins, Behavior of the coupling parameter under isochoric heating in a high-Z plasma, Phys. Rev. E **87**, 061101(R) (2013).

[54] M. Torrent, F. Jollet, F. Bottin, G. Zérah, and X. Gonze, Implementation of the projector augmented-wave method in the ABINIT code: Application to the study of iron under pressure, Comput. Mater. Sci. **42**, 337 (2008).

[55] T. Rangel, D. Caliste, L. Genovese, and M. Torrent, A wavelet-based projector augmented-wave (PAW) method: Reaching frozen-core all-electron precision with a systematic, adaptive and localized wavelet basis set, Comput. Phys. Commun. **208**, 1 (2016).

[56] A. H. Romero, D. C. Allan, B. Amadon, G. Antonius, T. Applencourt, L. Baguet, J. Bieder, F. Bottin, J. Bouchet, E. Bousquet, F. Bruneval *et al.*, ABINIT: Overview and focus on selected capabilities, J. Chem. Phys. **152**, 124102 (2020).

[57] S. Lehtola, C. Steigemann, M. J. Oliveira, and M. A. Marques, Recent developments in LIBXC–A comprehensive library of functionals for density functional theory, SoftwareX **7**, 1 (2018).